Atmospheric Environment 267 (2021) 118755

Contents lists available at ScienceDirect

Atmospheric Environment

journal homepage: www.elsevier.com/locate/atmosenv

Formation mechanism of HCHO pollution in the suburban Yangtze River Delta region, China: A box model study and policy implementations

Kun Zhang [a,b], Yusen Duan [c], Juntao Huo [c], Ling Huang [a,b], Yangjun Wang [a,b], Qingyan Fu [c], Yuhang Wang [d], Li Li [a,b,*]

[a] School of Environmental and Chemical Engineering, Shanghai University, Shanghai, 200444, China
[b] Key Laboratory of Organic Compound Pollution Control Engineering, Shanghai University, Shanghai, 200444, China
[c] Shanghai Environmental Monitoring Center, Shanghai, 200235, China
[d] School of Earth and Atmospheric Sciences, Georgia Institute of Technology, Atlanta, GA, USA

HIGHLIGHTS

- Photolysis of HCHO is a significant source of RO_x.
- Isoprene was found as a key precursor of HCHO.
- More active VOCs should be reduced to mitigate HCHO pollution in the YRD region.

GRAPHICAL ABSTRACT

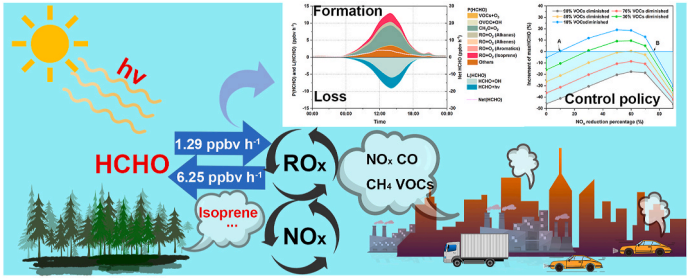

ARTICLE INFO

Keywords:
Formaldehyde
Box model
Photochemical reactions
Atmospheric oxidation capability

ABSTRACT

High levels of formaldehyde (HCHO) have been frequently detected during spring-summertime in the densely populated and rapidly developing Yangtze River Delta (YRD) region, China. However, the detailed formation mechanism of HCHO pollution remains unclear. Based on a comprehensive field campaign conducted at Dianshan Lake (DSL) station, a supersite located in the suburban YRD region, the influence of VOCs on HCHO formation, as well as the role of HCHO in the RO_x radical recycling was analyzed. Results indicate that the maximum atmospheric oxidation capability (AOC) during HCHO pollution episodes varies from 0.65×10^8 to 1.29×10^8 molecules cm^{-3} s^{-1}, and high AOC value favors the secondary formation of HCHO. Meanwhile, the photolysis of HCHO accounts for 21.2% of the primary RO_x, suggesting the significant role of HCHO in RO_x recycling. Isoprene was identified to be a key precursor of HCHO, and the RO from isoprene contributed ~15% to the total daytime HCHO production rate (P_{HCHO}). Sensitivity analysis reveal that when isoprene, xylene or ethylene was cut off, the simulated HCHO concentration could be reduced by 50%, 15%, or 13%, respectively. Based on the isopleth of HCHO under different VOCs/NO_x reduction ratios, we found that the VOCs/NO_x reduction ratio should be above 1.03 to mitigate the HCHO pollution. Reactive VOCs (such as isoprene, xylene and alkenes) should be reduced to suppress HCHO pollution in the YRD region.

* Corresponding author. School of Environmental and Chemical Engineering, Shanghai University, Shanghai, 200444, China.
E-mail address: lily@shu.edu.cn (L. Li).

https://doi.org/10.1016/j.atmosenv.2021.118755
Received 17 June 2021; Received in revised form 30 August 2021; Accepted 26 September 2021
Available online 29 September 2021

1. Introduction

Formaldehyde (HCHO) is the most abundant carbonyls in the atmosphere (Blas et al., 2019) and is a key precursor of ozone (O_3) (Li et al., 2010; Ling et al., 2017). Generally, HCHO can be directly emitted from anthropogenic sources (combustion processes, chemical industry, and consumer products, etc.) (Blas et al., 2019; Liu et al., 2009; Mason et al., 2001). The major source of HCHO, however, is the oxidation of volatile organic compounds (VOCs) (Atkinson, 2000; Atkinson and Arey, 2003; Blas et al., 2019; Wolfe et al., 2016a). Numerous measurements of ambient carbonyls have been conducted to explore their spatial and temporal characteristics over the world (Blas et al., 2019; Li et al., 2014b; Tang et al., 2019). In China, the seasonal averaged concentration of HCHO ranged from 4 ppbv to 24 ppbv in megacities (Zhang et al., 2019b). High levels of HCHO pollution have been detected in the Yangtze River Delta (YRD) region, Pearl River Delta (PRD) region, and North China Plain region (Zhang et al., 2019b). To differentiate the primary and secondary HCHO, Friedfeld et al. (2002) used a multi-linear regression model based on the relationship between HCHO and other trace gases (O_3 and CO). Similar method was also used in the studies conducted in China (Li et al., 2010). For example, Yang et al. (2017) reported that photochemical formation was an important source of HCHO at Mount Tai, China, accounting for ~44% of the total HCHO mass concentration.

As previous studies suggested, HCHO can be produced via the degradation processes of various precursors (Atkinson and Arey, 2003). For instance, HCHO is an important byproduct during the degradation of isoprene, which is the most abundant biogenic VOCs globally (Jenkin et al., 2015). In addition, Blas et al. (2019) reported that the HCHO mixing ratio at a rural site of France was highly correlated with O_3 and isoprene. Recently, many studies utilized the observation-based model (OBM) coupled with measurement data to investigate the detailed formation mechanism of HCHO (Wolfe et al., 2016a; Yang et al., 2017, 2020). For example, Li et al. (2014b) investigated the production pathways of HCHO at a semi-rural site of China and found that isoprene contributed most to the HCHO production (43%), followed by alkenes (29%), and aromatics (15%). However, in urban areas, anthropogenic emissions (e.g., alkenes) could be the dominant source (54%) of HCHO. These differences could be attributed to local emission characteristics since the yield of HCHO from isoprene is highly NO_x-affected (Wennberg et al., 2018). For instance, over a range of 0.1–2 ppbv of NO_x, there will be a threefold increase in the HCHO yield from isoprene (from 0.3 to 0.9 ppbv h^{-1}) (Wolfe et al., 2016a). Therefore, identification of the dominant precursors and investigation of the HCHO-precursor relationship are essential in understanding the formation mechanism of HCHO, which further guides the control policies.

The YRD region, as one of the fastest developing city-clusters in eastern China, has been suffering from severe O_3 and HCHO pollution, especially in recent years (Zhang et al., 2019a, 2020, 2021; Xu et al., 2020). Su et al. (2019) reported that the daily average HCHO level could exceed 18 ppbv at Dianshan Lake (DSL) site. However, the detailed formation mechanism of HCHO over the YRD region remains unclear. In this study, a comprehensive field campaign was conducted. We first show the temporal changes of various trace gases and meteorological parameters during the observation. Then five episodes with high HCHO concentrations (with peak value over 15 ppbv) were identified. A box model coupled with Master Chemical Mechanism (MCM) v3.3.1 was applied to further investigate the formation pathways of HCHO during these episodes. Additionally, the atmospheric oxidization capability (AOC), OH reactivity, RO_x budget, and series of sensitive tests were performed to better illustrate the formation of secondary HCHO. Finally, suitable VOCs/NO_x abatement ratio was proposed based on the simulations. This study could enhance our understanding of the formation pathways of HCHO at suburban areas and provides scientific basis for the control of HCHO.

2. Methodology

2.1. Field measurement

The field experiment was conducted at a monitoring site (120.98°E, 31.09°N) in the suburban area of YRD region, China, covering the period from 1st May to May 22, 2018 (Fig. 1). The site is surrounded by Dianshan Lake and several villages (Fig. S1) with low population density and is about 40 km away from the built-up center of Shanghai. Detailed information of this site has been described elsewhere (Zhang et al., 2020). Hourly averaged meteorological parameters (e.g., temperature (T), relative humidity (RH), atmospheric pressure (P), wind speed (WS) and wind direction (WD)) were captured by a meteorological station (Vaisala, Model CL31, FIN), while hourly-averaged atmospheric boundary layer (ABL) height was observed by a ceilometer (Vaisala, FIN). HCHO was measured by a Hantzsch fluorescence technique (AL4201, Aerolaser GmbH., GER). The analysis principle of HCHO is based on Hantzsch reaction: gaseous HCHO is transferred firstly into liquid phase and combines with acetone and ammonia to produce 3, 5-diacetyl-1,4-dihydrolutidine (DDL), which can be stimulated at a 410 nm wavelength and emits fluorescence, which is further detected by a photomultiplier. Trace gases (e.g., O_3, NO/NO_2, SO_2, and CO) were measured by a set of commercial instruments (Table S1). O_3 was measured by an ultraviolet photometric analyzer (Thermo Scientific, Model 49i, USA), with detection limit of 1 ppbv (10 s average); NO and NO_2 was monitored using a chemiluminescent analyzer (Thermo Scientific, Model 42i, USA); SO_2 was detected by a pulsed fluorescence analyzer (Thermo Scientific, Model 43i, USA); and CO was measured with a gas filter correlation analyzer (Thermo Scientific, Model 48i, USA). Total of 55 VOCs species, including 28 alkanes, 10 alkenes (including isoprene), 16 aromatics, and acetylene, were analyzed by two online gas chromatographs (GC) with flame ionization detector (FID) systems (GC-866 airmoVOC C2–C6 #58850712 and airmoVOC C6–C12 #283607112, Agilent., USA). The detection limit of trace gases and individual VOCs and more details about the observation data quality control can be found in Text S1, Table S1 and S2.

2.2. Observation-based model

An observation-based model with the newest version of MCM (v3.3.1; http://mcm.leeds.ac.uk/MCM/, last access: 24 May 2021) was applied to reflect the detailed photochemical processes and the production of HCHO at DSL site. The MCM v3.3.1 includes more than 5800 chemical species and 17000 reactions. In this model, dry deposition and dilution mixing within the boundary layer are also considered. The observed concentrations of NO, NO_2, O_3, CO, individual VOC species and meteorological parameters (T, RH, P, and ABL) were used in this model to constrain the simulation. The photolysis frequencies (J values) were calculated based on the trigonometric parameterization method provided by MCM and the detailed description of this method can be found elsewhere (Wolfe et al., 2016b). The horizontal and vertical transport of air masses was not included in this model. Before each simulation, the model was run 2 days as spin up to approach a steady state for unmeasured species (e.g., OH, HO_2 and RO_2 radicals). To quantitatively assess the performance of HCHO simulation, the index of agreement (IOA) was used, which is calculated by Equation (1) (Huang et al., 2005):

$$IOA = 1 - \frac{\sum_{i=1}^{n}(O_i - S_i)^2}{\sum_{i=1}^{n}\left(\left|O_i - \overline{O}\right| \pm \left|S_i - \overline{O}\right|\right)^2} \quad (1)$$

where O_i, S_i, and $\overline{O}$ are the concentration of observed, simulated, and averaged HCHO concentrations, respectively. The calculated IOA value was 0.70, which was comparable to the results reported in previous studies (Lyu et al., 2016; Wang et al., 2017, 2018; Zeng et al., 2019),

indicating that the simulation of this model was reasonable.

AOC, which plays a vital role in converting primary pollutants into secondary ones, was calculated based on the explicit simulation (Equation (2)):

$$AOC = \sum_i k_{Y_i}[Y_i][X] \quad (2)$$

where Y_i represents VOCs, CO, and CH_4; X are oxidants (OH, O_3, and NO_3); k_{Yi} is the bimolecular rate constant for the reaction of Y_i with X (Elshorbany et al., 2009; Xue et al., 2016). Additionally, OH reactivity, which is widely used as an indicator of atmospheric oxidation intensity, was also calculated based on the results of OBM (Equation (3)):

$$k_{OH} = \sum_i k_{OH+X_i}[X_i] \quad (3)$$

where $[X_i]$ is the concentration of species i (e.g., NO_2, CO, VOCs) and $k_{OH + Xi}$ is the bimolecular rate constant for the reaction of OH and X_i.

3. Results and discussion

3.1. Overview of observation

During the observation, the average T and RH was 295.5 ± 5.1 K, and 76 ± 18%, respectively, indicating warm and moist weather conditions. These meteorological conditions, together with the emissions of air pollutants, were in favor of high photochemical reactivity. A detailed summary of key meteorological parameters and trace gases can be found in Table S3. Under such conditions, the maximum O_3 concentration reached 155 ppbv on 18th May. According to the Chinese National Ambient Air Quality Standards (NAAQS), the grade II threshold of maximum daily 8-h average (MDA8) of O_3 is 160 μg/m^3 (~75 ppbv). During the whole campaign, 13 days were found with MDA8 over 75 ppbv, suggesting severe photochemical pollution during spring-summer season in this region. As for HCHO, the average value was 6.7 ± 3.6 ppbv, with the maximum of 20.9 ppbv observed on 13th May. Additionally, during the observation period, relatively high density of column HCHO was found in eastern China (Fig. S2). Which was consistent with previous studies (Zhang et al., 2019b). Currently, there is no standard formulating the threshold of outdoor HCHO concentration, we use the 95th percentile concentration of HCHO (15 ppbv), as a threshold to screen high HCHO days. During the observation period, five HCHO pollution episodes (12th ~15th and May 18, 2018) with peak HCHO concentrations exceeding 15 ppbv were selected (gray shadow in Fig. 2). During the HCHO pollution episodes, the average T and O_x ($O_x = O_3 + NO_2$) was 298.8 ± 4.1 K and 68.6 ppbv, respectively, which was 4.4 K and 9.2 ppbv higher than non-episode days. Blas et al. (2019) concluded that increases in temperature are always linked with higher radiation and larger biogenic isoprene emissions, which is a key precursor of HCHO. Additionally, the overlap of O_3 and HCHO pollution and the relatively higher O_x concentrations during HCHO episodes indicated the fast photochemical formation of HCHO during daytime (Fig. 2). Therefore, the relatively higher temperature and atmospheric oxidation capability promoted the secondary formation of HCHO during episodes. It should be noted that the average CO and SO_2 concentration was 658 ppbv and 4.1 ppbv during the episodes, which was 164 and 1.0 ppbv higher than that during non-episode days. This implied stronger anthropogenic emissions as well as the pollution accumulation under unfavorable meteorological conditions during the HCHO episodes.

3.2. Formation of HCHO

The simulated and observed concentrations of HCHO in each episode are given in Fig. 3 (a). During the five episodes, the daily average wind speed varies from 1.4 to 2.7 m/s, suggesting the HCHO episodes generally occurred under stagnant conditions. Hence, the OBM is suitable for following discussions, which focus on reaction rate analysis. It should be noted that there was some discrepancy between the simulated and observed HCHO concentration. This could be partially attributed to the limitation of the OBM model, which only considers the photochemical reactions, dry deposition and dilution mixing within the boundary layer, while the primary emissions of HCHO and the transport of air masses are not considered. Although there is certain discrepancy, the model could generally reflect changes of the HCHO pollution (as illustrated by Fig. 3(a)), with IOA between observed and predicted value of 0.7, similar to previous published literature (Lyu et al., 2016; Wang et al., 2017, 2018; Zeng et al., 2019). Therefore, the model results are acceptable. Furthermore, to reveal the influence of primary emissions on the simulated HCHO value, the concentrations of CO and SO_2, which are primary pollutants, were used to represent the strength of primary emissions. As shown in Fig. 2 and Fig. S3, increased anthropogenic emissions were identified during the HCHO episodes, and the overlaps of the peaks of CO/SO_2 and HCHO during May 12th ~14th and May 18th suggests that primary emissions could influence the observed HCHO concentrations and lead to deviations between simulation and observations. The simulated HCHO exhibited a decreasing trend to around 5 ppbv before dawn. After sunrise, the air temperature increases, leading to fast development of atmospheric boundary layer (Fig. 3 (a)). Meanwhile, active photochemical reactions lead to accumulation of HCHO. After midday, the net production of HCHO decreases gradually and the simulated HCHO peaks around 15:00 with concentrations of 16.56–24.20 ppbv, followed by a decrease of HCHO to 1.14–9.19 ppbv at night. During the HCHO episodes, a positive relationship between T

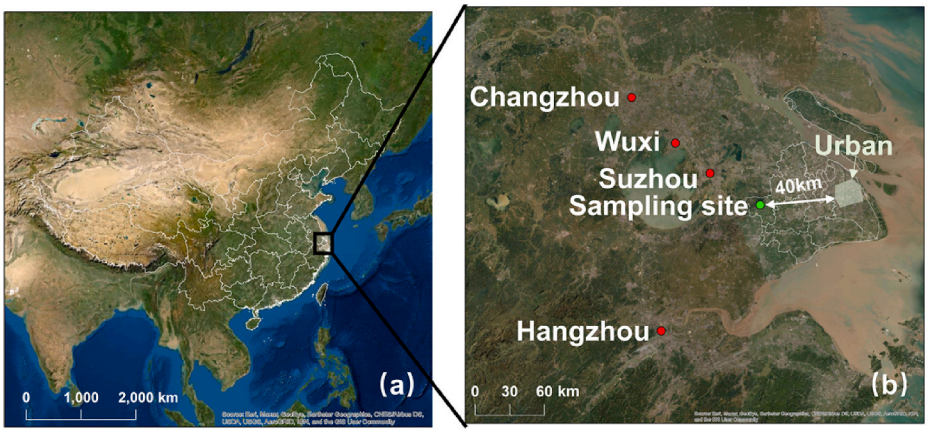

Fig. 1. (a) Map of China; (b) Location of the sampling site (green point), nearby cities (red points) and shape of urban Shanghai (gray shaded area). (For interpretation of the references to colour in this figure legend, the reader is referred to the Web version of this article.)

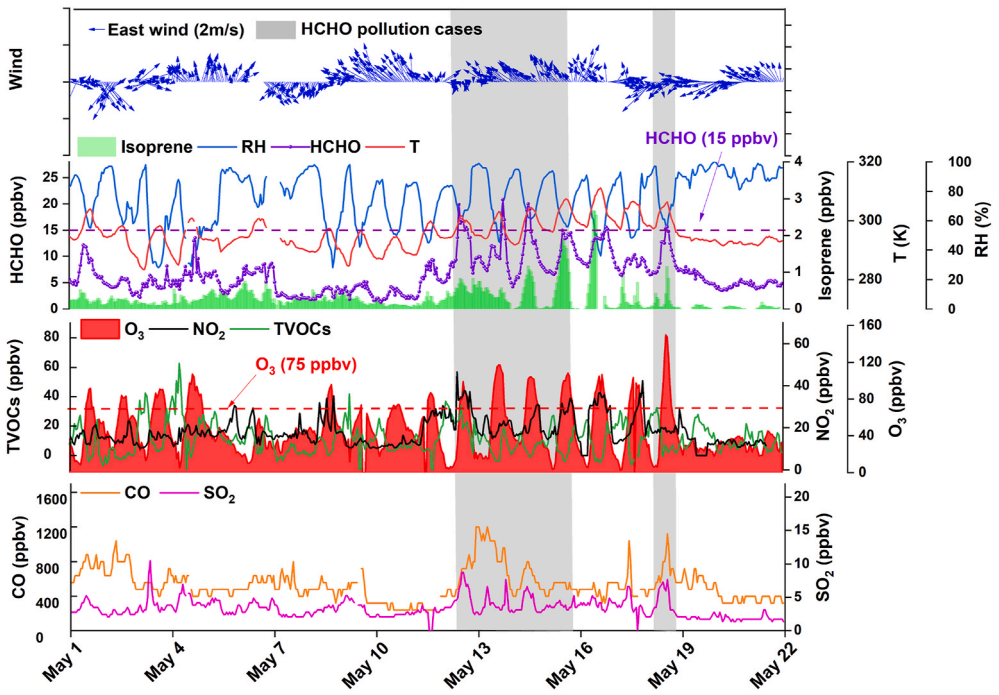

Fig. 2. Time series of major meteorological parameters and trace gases from 1 May to May 22, 2018. The purple and red dash lines represent HCHO of 15 ppbv and O_3 of 75 ppbv. The two shaded areas represent typical HCHO pollution cases. (For interpretation of the references to colour in this figure legend, the reader is referred to the Web version of this article.)

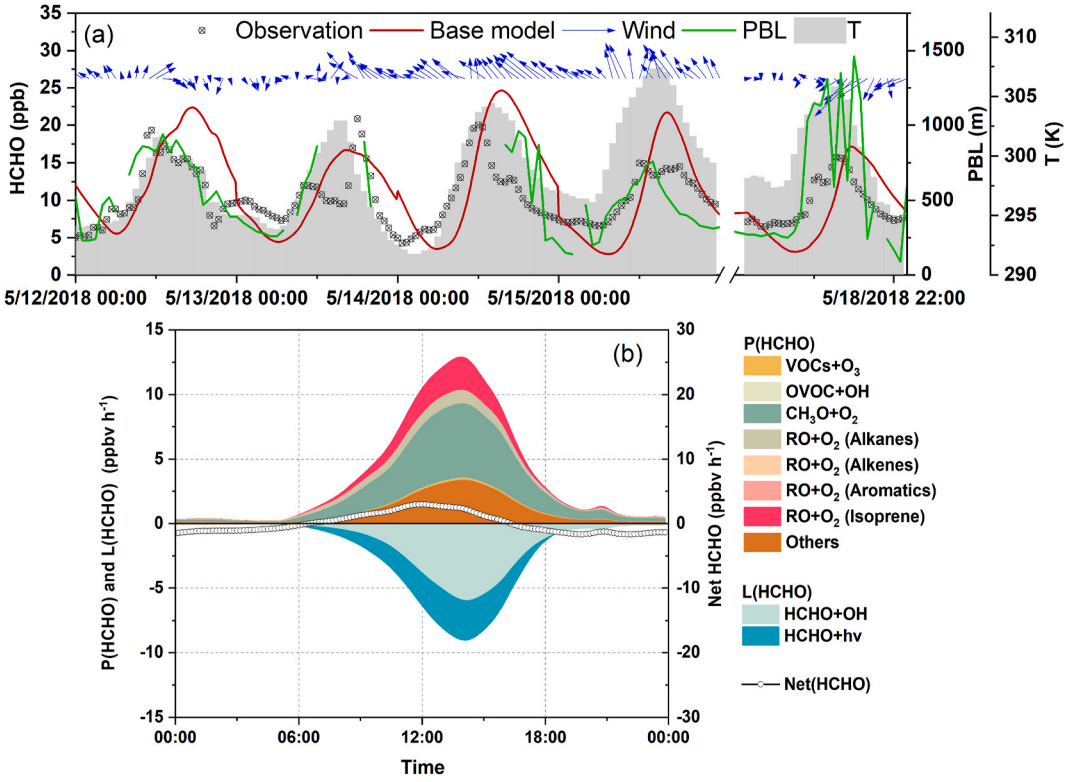

Fig. 3. (a) Simulated and observed concentration of HCHO during HCHO pollution cases. (b) Average diurnal variation of the formation and loss pathways of HCHO during HCHO pollution cases.

and the simulated HCHO is found, with a correlation coefficient of 0.439 ($p < 0.01$), suggesting the promoting effect of temperature on HCHO formation. Relatively higher T was found on May 15th and May 18th but the simulated and observed HCHO was much lower than the other 3 episodes. This could be attributed to the lower OH concentrations (Fig. S4), which further restrained the formation of HCHO. Based on the explicit mechanism of MCM, we are able to investigate the formation and loss pathways of HCHO (Fig. 3 (b)). Since the formation and loss of

HCHO mainly happened during daytime, the following discussion focuses on daytime results. The average production pathways (P_{HCHO}) of HCHO exhibited a unimodal diurnal variation, with an increasing rate after sunrise and a peak value around 14:00. By breaking down P_{HCHO}, we found $CH_3O + O_2$ alone made a significant contribution of ~48% to the formation of HCHO, with a daytime average reaction rate of 3.18 ± 1.88 ppbv h^{-1}. The dominant contribution of CH_3O to HCHO was also reported in previous studies (Li et al., 2014b; Yang et al., 2020; Zhu et al., 2020). Since CH_3O radical could be produced during the degradation of anthropogenic-related VOCs (aromatics and alkenes) and biogenic-related VOCs (isoprene), the secondary formation of HCHO at DSL site could be jointly controlled by biogenic and anthropogenic emissions. It is notable that the RO from isoprene can also contribute ~15% to total P_{HCHO} rate. As suggested by previous studies, isoprene degradation could be the dominant source in semirural areas (Li et al., 2014a). As a suburban site with high vegetation coverage, the important role of isoprene in HCHO formation is expected at DSL site. In addition, the reaction of alkene-derived radicals and O_2 also contributed ~10% to total HCHO production rate. As for the sink pathways of HCHO (L_{HCHO}), the reaction of HCHO + OH, forming HO_2 and CO, was the dominant channel, with an average contribution of ~62%. In addition, the photolysis of HCHO can also efficiently scavenge HCHO, with an average daytime reaction rate of 1.69 ± 1.04 ppbv h^{-1}. The average net production of HCHO ($NET_{HCHO} = P_{HCHO} + L_{HCHO}$), shown in Fig. 3 (b), increased after sunrise and reached the maximum value (4.16 ppbv h^{-1}) at around 12:00 a.m. During daytime, the positive NET_{HCHO} value indicates the accumulation of HCHO.

3.3. Atmospheric oxidization capability

Atmospheric oxidization capacity plays a significant role in the degradation of VOCs and the subsequent formation of secondary pollutants (such as HCHO, secondary organic aerosols and O_3). Therefore, we calculated the AOC in the five identified episodes (shown in Fig. 4 (a)) according to Equation (2). Overall, the profile of AOC exhibited a similar diurnal variation, with a peak at about 13:00. The maximum AOC in each episode varies from 0.65 × 10^8 to 1.29 × 10^8 molecules cm^{-3} s^{-1}. Comparatively, the AOC values are close to those computed for urban environment of Shanghai and Hongkong, with a range of 8.8 × 10^7–1.0 × 10^8 molecules cm^{-3} s^{-1} and 1.27 × 10^8–2.04 × 10^8 molecules cm^{-3} s^{-1}, respectively (Zhu et al., 2020; Xue et al., 2016). However, they are much lower than the AOC level at Santiago de Chile (Elshorbany et al., 2009) and Berlin (Geyer et al., 2001). The peak AOC changed as the OH concentration changed (Fig. S4), suggesting the dominant role of OH in AOC, which was also found in Shandong (Chen et al., 2020), Beijing, Guangzhou and Chongqing (Tan et al., 2019). The second most important oxidant is O_3, accounting for 3.16%–33.14% of total AOC, with an average value of 1.62 ± 0.95 × 10^6 molecules cm^{-3} s^{-1}. NO_3 can become an important oxidant during nighttime, which is consistent with the results of Zhu et al. (2020). Therefore, the reactions between primary pollutants and OH were the dominant processes producing secondary pollutants in these cases.

Furthermore, we compared the contribution of different reactants to the loss of OH using OH reactivity (k_{OH}, shown in Fig. 4 (b)). The maximum k_{OH} varied from 22.57 to 36.09 s^{-1}, with the maximum value observed on 12th May. Results indicate that OVOCs were the dominant contributor (~38%) to k_{OH}, especially on 12th May and 14th May, when OVOCs contributed 41.4% and 44.9% to the total k_{OH}, respectively. Comparatively, similar results were found at VOCs-rich areas in Shandong, China, indicating that OVOC can contribute 69.1 ± 7.2% to total k_{OH} (Chen et al., 2020). However, our result is much higher than the simulation for urban areas of Shanghai, which suggested that the CO and NO_2 dominates k_{OH} (Zhu et al., 2020). This difference can be attributed to the abundant CO and NO_x emission in urban areas (Zhu et al., 2020). It should be noted that the breakdown of k_{OH} from OVOC indicates that HCHO can account for 8.5%–14.3% of total k_{OH} in the 5 episodes, with

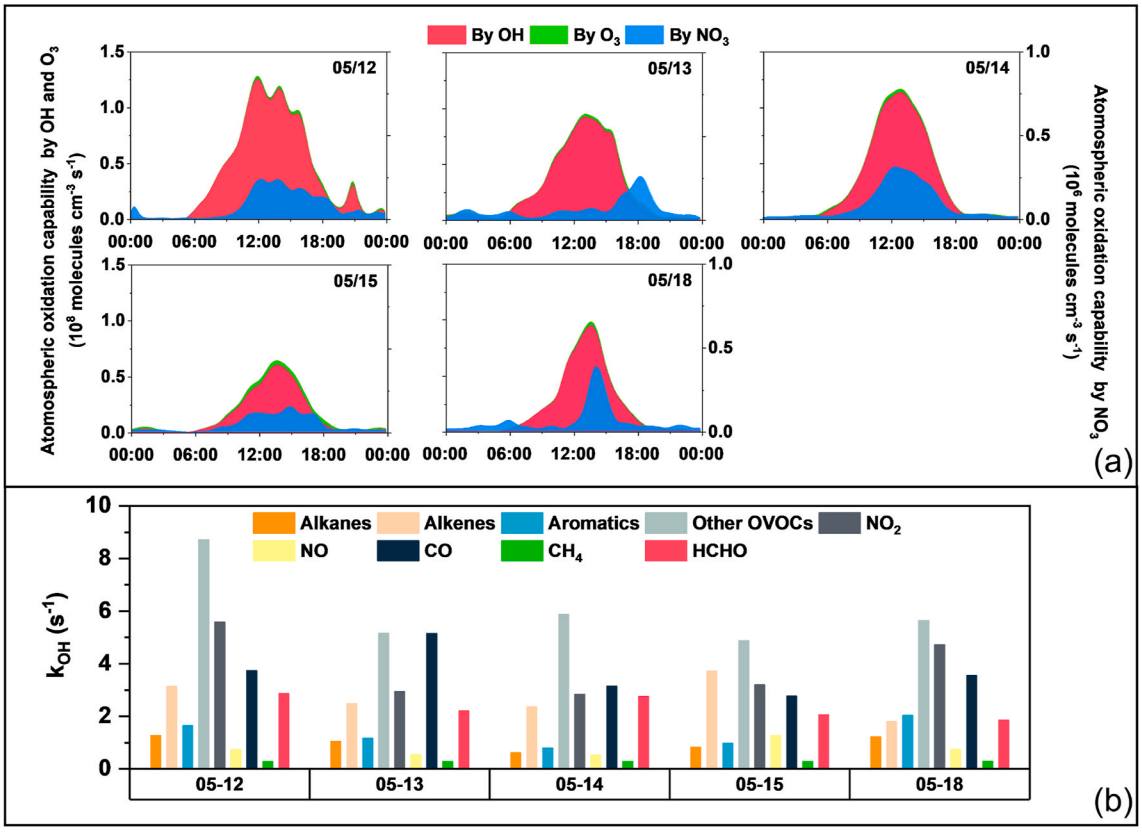

Fig. 4. (a) Simulated atmospheric oxidization capability in typical cases. (b) Breakdown of OH reactivity in each episode (s^{-1}).

k_{OH} value ranging from 1.85–2.87 s^{-1}, suggesting the significance of HCHO in atmospheric photochemistry and ozone generation. This is consistent with the results of Zeng et al. (2019), which suggested that diminishing HCHO can reduce as much as 30.7 ± 9.0% of the peak net O_3 rate in Wuhan, China. The NO_2 and CO were the second and third important contributor to k_{OH}, with an average contribution percentage of 17.29 ± 3.31% and 16.88 ± 4.50%, respectively. These results are relatively lower than that simulated for urban areas of Shanghai (33% and 21%, respectively (Zhu et al., 2020),). The k_{OH} from hydrocarbons was dominated by alkenes, with a contribution ranging from 1.80 to 3.71 s^{-1}, which was attributed to the relatively higher reactivity of alkenes. The k_{OH} from alkanes and aromatics were comparable in each case, with an average value of 0.99 ± 0.27 and 1.32 ± 0.50 s^{-1}, respectively. Since CH_4 is relatively inert, the contribution of CH_4 to total k_{OH} was only 1.44 ± 0.24%, with a maximum k_{OH} value of 1.79 s^{-1}. Therefore, the reactions between OH and reactive air pollutants (e.g., HCHO, NO_2) dominated the fate of OH.

3.4. RO_x budget analysis

Since the fate of air pollutants (especially VOCs and OVOCs) is closely linked with RO_x, the breakdown of daytime source and sink pathways of RO_x (including the photolysis of O_3, HNO_3, HONO, OVOC, and HCHO) is calculated to investigate the impact of HCHO on RO_x budget (shown in Fig. 5). In Fig. 5, the red, blue, and green lines indicate the primary sources, sink pathways, and the recycling of RO_x, respectively. According to Fig. 5 (a), photolysis of O_3 was the dominant primary source of OH during daytime, with a peak rate value of 1.28 ppbv h^{-1} at around 12:00. However, photolysis of HONO could become an important OH source during early morning, when the concentration of HONO was abundant and the generation of O_3 was not active. This suggests that O_3 photolysis dominates OH production under high O_3 conditions, while HONO photolysis is more significant at low O_3 conditions (Wang et al., 2018; Zhu et al., 2020). It is worth noting that the contribution of HONO photolysis to total primary source of OH is much lower than previous studies (Liu et al., 2012; Yang et al., 2021; Liu et al., 2021). This could be attributed to the constrain of HONO concentration in our model, since HONO is produced from the homogenous process of OH + NO or heterogeneous conversion of NO_2, or contributed by other sources (such as direct emissions and unknown sources) (Liu et al., 2020; Liu et al., 2021), which are not included in our simulation. Therefore, the simulation could underestimate the concentration of HONO and further underrate the rate of HONO photolysis. Other minor sources of OH, such as OVOC photolysis only contributed ~3% of the primary source of OH. For RO_2, the most important source is photolysis of OVOCs (excluding HCHO), with a daytime average production rate of 1.30 ppbv h^{-1}, which was similar to the results of Xue (2016). For HO_2, the photolysis of HCHO and other OVOCs are the two dominant primary sources, with average daytime rate of 0.56 and 0.73 ppbv h^{-1}, respectively.

From the perspective of RO_x, the primary radical production was dominated by the photolysis of OVOCs (except for HCHO), followed by the photolysis of HCHO and O_3 (Fig. 5 (d)). This result is consistent with previous studies (Chen et al., 2020; Liu et al., 2012). It is worth noting that HCHO accounted for 21.2% of the total RO_x production. This value is comparable to previous studies (Chen et al., 2020; Zhu et al., 2020), and indicated that HCHO could strongly affect the total RO_x concentration by influencing the concentration of HO_2 radical, especially during midday (Fig. 5 (c)). With the co-existence of abundant NO_x and VOCs, the radical propagation was efficient and could amplify the effect of newly produced radicals in the polluted atmospheres (Xue et al., 2020). As for the sink of RO_x, the reaction of OH + NO_2 forming HNO_3 at an average rate of 2.34 ppbv h^{-1} was the most important pathway (Fig. 5 (d)). Other sink pathways (e.g., HO_2+RO_2, NO + OH, RO_2+NO_2) contributed ~46% of the total sink rates of RO_x. Overall, the reactions of NO_x + RO_x dominated the termination of RO_x.

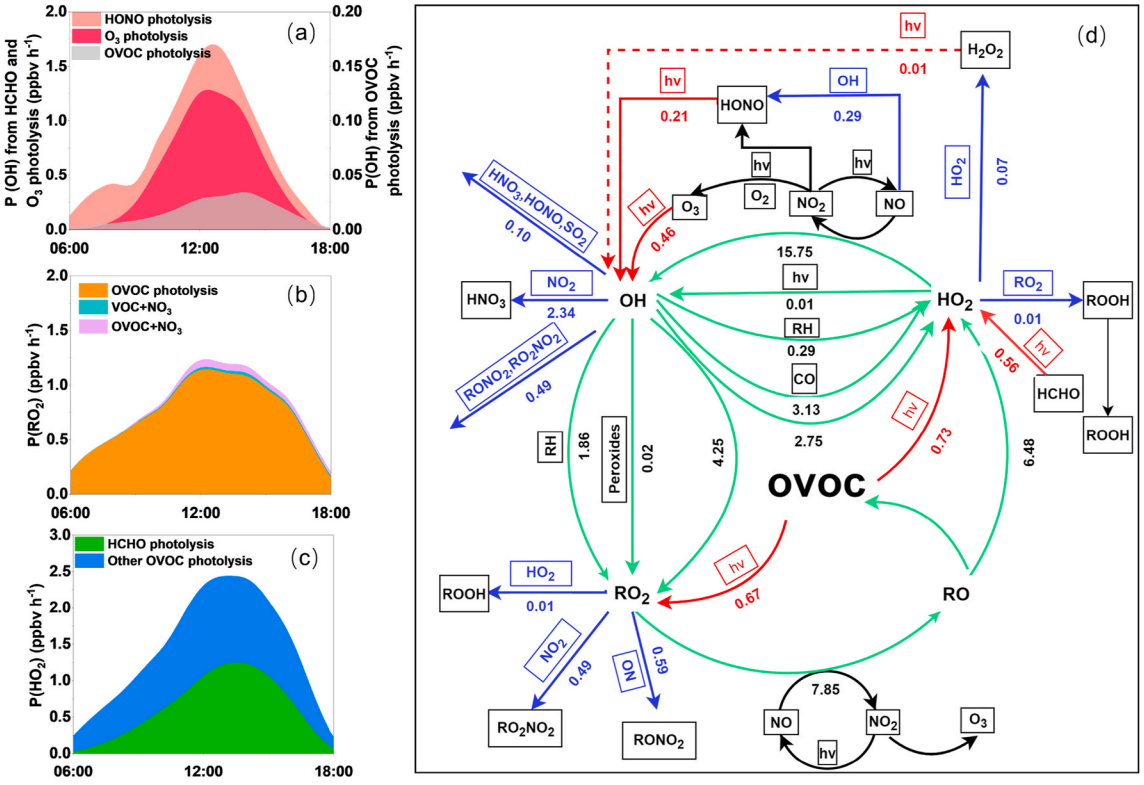

Fig. 5. Breakdown of average daytime production pathways of OH (a), RO_2 (b) and HO_2 (c). (d) Daytime average RO_x budget in 5 HCHO pollution cases. The unit is ppbv h^{-1}. The green, red, and blue lines indicate the recycling, primary production, and sink pathways of RO_x, respectively. (For interpretation of the references to colour in this figure legend, the reader is referred to the Web version of this article.)

3.5. Identification of key precursors of HCHO

As suggested in Fig. 3 (b), the formation of HCHO could be significantly affected by VOCs, especially alkenes and aromatics. To quantitatively assess the sensitivity of HCHO formation to different VOC species and provide more information for the formulation of HCHO control policies, 7 scenarios (eliminating the input of toluene, ethylbenzene, xylene, benzene, isoprene, ethylene, and propylene, respectively) were simulated and the results are summarized in Table 1. Interestingly, the secondary formation of HCHO was most sensitive to isoprene, with a drop of 50% in HCHO concentration when eliminating isoprene input. This result is in line with the study carried out in Beijing (Yang et al. (2017)). Meanwhile, eliminating other anthropogenic alkenes (ethylene and propylene), xylene and ethylene could lead to similar reduction ratio of HCHO, ranging from 10%–15%. Then we calculated the changes of OH, RO_2, and HO_2, which serve as vital oxidant in the formation of HCHO, in each simulation. Results indicate that eliminating isoprene could lead to a decrease of 48%, 24%, and 46% in RO_2, OH, and HO_2, respectively. As suggested by Zhang et al. (2021), eliminating active VOC species (such as isoprene) could significantly restrain the RO_x recycling rate and further pull-down the concentration of RO_x. Additionally, cutting off active aromatics (toluene and xylene) and alkenes (ethylene and propylene) can also lead to significant reduction in RO_2, OH and HO_2, with a range of −16% ~ −26%, −11% ~ −16%, −18% ~ −26%, respectively. Taking scenario 5 as an example, eliminating isoprene could significantly reduce OH and HO_2 concentrations, and then lead to the decrease of CH_3O, aromatics-derived RO (ARORO) and isoprene-derived RO (ISORO) concentrations by 45%, 21% and 100%, respectively, and finally cause ~50% reduction of HCHO. Therefore, isoprene, xylene, toluene, ethylene, and propylene are the key precursors of HCHO in this region.

3.6. Development of the optimum control policies on VOCs and NO_x

The concentrations of NO_x and VOCs strongly influence the recycling of RO_x (shown in Fig. 5 (d)) and the generation of HCHO. Therefore, the control policies of HCHO should consider abatement in both NOx and VOCs. To calculate the changes in maximum HCHO (maxHCHO), May 14th was chosen to perform Empirical Kinetics Modeling Approach (EKMA) analysis, since the average HCHO concentration on this day was the highest among the five cases and it exhibited unimodal diurnal variation during this episode. To quantify how much NOx and VOCs are necessarily to be reduced to diminish HCHO pollution, the isopleths of maxHCHO with the reduction of both VOCs and NOx were calculated (Fig. 6 (a)). In Fig. 6 (a), the horizontal and the vertical axis represent the percentage of the measured mean NOx and VOCs concentration, respectively. The ridge of the isopleth, with the NOx/VOCs ratio of 1:10, dividing this figure into two regimes. Above this ridge, the formation of HCHO was VOC-limited. Conversely, below this ridge, the formation of HCHO was NOx-limited. It was found that the formation of HCHO in this episode was in the VOC-limited regime (with 100% of VOCs and NOx as input, shown as white point in Fig. 6 (a)). Reducing VOCs could lead to monotonically decrease of maxHCHO (bule line in Fig. 6 (a) and (b)); however, eliminating NOx could firstly increase maxHCHO, and then lead to dramatic reduction of HCHO when over 50% NOx was diminished (red line in Fig. 6 (a) and (c)). Additionally, the variation of maxHCHO under 1:20, 1:10 and 1:5 NOx/VOCs reduction ratios were also calculated (green, gray, and pink lines in Fig. 6 (a) and (c)). It was found that the higher NOx/VOCs reduction ratios lead to more slowly decrease rate of maxHCHO (Fig. 6 (c)). Therefore, more efforts should be paid to the reduction of major VOCs precursors to reduce HCHO pollution.

However, VOCs and NOx are usually simultaneously controlled in practice. To investigate how much NOx and VOCs should be reduced to alleviate HCHO pollution, the maxHCHO under different VOCs and NOx reduction percentage were calculated (Fig. 6 (d)). It is found that the maxHCHO increased as the reduction percentage of NOx increased from 0% to 60%, regardless of VOCs, while maxHCHO decreased gradually when over 60% NOx was diminished. Interestingly, when >60% VOCs were reduced, the reduction of NOx would lead to net decrease of maxHCHO. It should be noted that, when the reduction percentages of VOCs range from 10% to 30%, the decrease of NOx should be 0–28% or 76%–100% to avoid net increase of maxHCHO. It was determined that when the reduction percentages of NOx ranges from 0% to 90%, the minimum abatement ratio of VOCs/NOx should be > 1.03 or < 0.13 (i.e., the abatement ratios of VOCs/NOx at the intersections of the curves and the horizontal axis, shown as point A and B in Fig. 6 (d)). However, reducing NOx by 76%–100% may not be feasible currently in practice. Therefore, we focus on the range of 0–76% of NOx reduction and the abatement ratio of VOCs/NOx should be higher than 1.03 to reduce the HCHO concentration at DSL site.

4. Conclusions

HCHO is a key trace gas contaminant generated during the degradation of VOCs. Based on the simultaneous observation of HCHO, VOCs, and meteorological parameters, we analyzed the production and destruction pathways of HCHO for 5 identified episodes at a suburban site in the YRD region, China, during spring-summertime. High AOC levels (0.65×10^8 to 1.29×10^8 molecules cm^{-3}), dominated by OH radicals, were found during the daytime and offered suitable condition for photochemical reactions during these episodes. The photolysis of OVOCs, especially HCHO, is the key source of RO_x and accounted for 22% of the total RO_x sources. The breakdown of the HCHO formation pathways suggested that the HCHO formation at DSL was influenced by both anthropogenic and biogenic emissions. Among all the observed VOCs, isoprene contributes the most to the secondary formation of HCHO, with an average contribution of ~15%. Sensitivity analysis suggests that eliminating isoprene can strongly influence the RO_x level, which further leads to 50% reduction of simulated HCHO. The EKMA analysis suggests that the formation of HCHO at DSL during spring-summertime was in VOC-limited regime and reducing VOCs could lead to monotonically decrease of maxHCHO. However, improper abatement ratio of VOCs and NO_x could lead to increase of HCHO. To prevent the increase of HCHO at DSL site, the abatement ratio of VOCs/NOx should be higher than 1.03. In summary, this study emphasized the important role of HCHO in the recycling of RO_x and underscored the effect of active VOCs (especially isoprene) in the secondary formation of

Table 1
Summary of simulated changes of radicals, HCHO and OVOCs concentrations in different scenarios.

Scenario	Eliminated factor	ΔHCHO (%)	ΔRO_2 (%)	ΔOH (%)	ΔHO_2 (%)	ΔCH_3O (%)	ΔARORO[a] (%)	ΔISORO[a] (%)
1	Toluene	−10	−21	−13	−21	−18	−40	−13
2	Ethylbenzene	−5	−14	−10	−15	−11	−16	−11
3	Xylene	−15	−26	−16	−26	−27	−36	−14
4	Benzene	−4	−12	−9	−13	−9	−8	−11
5	Isoprene	−50	−48	−24	−46	−45	−21	−100
6	Ethylene	−13	−16	−11	−18	−12	−9	−12
7	Propylene	−12	−18	−12	−18	−17	−9	−12

[a] ARORO and ISORO are the abbreviation of RO from aromatics and isoprene, respectively.

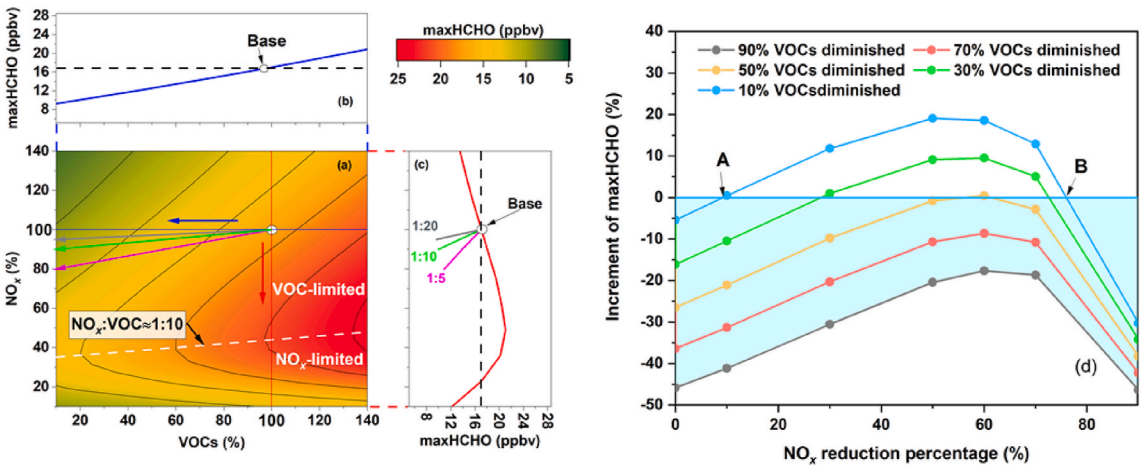

Fig. 6. (a) The maxHCHO isopleth in term of percentage changes of VOCs and NO_x. The white point represents the base scenario. (b) The variation of maxHCHO as a function of reduction percentage of VOCs. (c) The variation of maxHCHO as a function of reduction of NO_x. (d) Increment of maxHCHO as a function of reduction percentage of NOx and VOCs. The gray, green, and pink arrows in (a) represent the reduction route with NO_x/VOC ratio of 1:20, 1:10, and 1:5, respectively, and the gray, green and pink lines in (c) correspond to the change in maxHCHO. The black dash line in (b) and (c) represent the maxHCHO level in the base case. (For interpretation of the references to colour in this figure legend, the reader is referred to the Web version of this article.)

HCHO. Results of this study are helpful for the development of control strategies to mitigate the severe photochemical pollution in China.

Author statement

Kun Zhang: Formal analysis, Methodology, Writing-original draft. Juntao Huo: Formal analysis, Data curation. Yusen Duan: Formal analysis, Data curation. Qingyan Fu: Formal analysis. Ling Huang: Writing-review. Yuhang Wang: Writing-review. Elly Yaluk: Formal analysis. Li Li: Conceptualization, Methodology, Writing-review & editing.

Declaration of competing interest

The authors declare that they have no known competing financial interests or personal relationships that could have appeared to influence the work reported in this paper.

Acknowledgements

This study is supported by the National Natural Science Foundation of China (NO. 42075144, 41875161, 42005112), Shanghai Science and Technology Fund (No. 19DZ1205007), Shanghai International Science and Technology Cooperation Fund (No. 19230742500), and Shanghai Sail Program (19YF1415600), and the National Key Research and Development Program of China (NO. 2018YFC0213600). Y. Wang was supported by the National Science Foundation.

Appendix A. Supplementary data

Supplementary data to this article can be found online at https://doi.org/10.1016/j.atmosenv.2021.118755.

References

Atkinson, R., 2000. Atmospheric chemistry of VOCs and NO_x. Atmos. Environ. 34, 2063–2101.
Atkinson, R., Arey, J., 2003. Atmospheric degradation of volatile organic compounds. Chem. Rev. 103, 4605–4638.
Blas, M., Ibanez, P., Garcia, J.A., Gomez, M.C., Navazo, M., Alonso, L., Durana, N., Iza, J., Gangoiti, G., de Camara, E.S., 2019. Summertime high resolution variability of atmospheric formaldehyde and non-methane volatile organic compounds in a rural background area. Sci. Total Environ. 647, 862–877.
Chen, T., Xue, L., Zheng, P., Zhang, Y., Liu, Y., Sun, J., Han, G., Li, H., Zhang, X., Li, Y., Li, H., Dong, C., Xu, F., Zhang, Q., Wang, W., 2020. Volatile organic compounds and ozone air pollution in an oil production region in northern China. Atmos. Chem. Phys. 20, 7069–7086.
Elshorbany, Y.F., Kurtenbach, R., Wiesen, P., Lissi, E., Rubio, M., Villena, G., Gramsch, E., Rickard, A.R., Pilling, M.J., Kleffmann, J., 2009. Oxidation capacity of the city air of Santiago, Chile. Atmos. Chem. Phys. 9, 2257–2273.
Friedfeld, S., Fraser, M., Ensor, K., Tribble, S., Rehle, D., Leleux, D., Tittel, F., 2002. Statistical analysis of primary and secondary atmospheric formaldehyde. Atmos. Environ. 36, 4767–4775.
Huang, J., Fung, J., Lau, A., Qin, Y., 2005. Numerical simulation and process analysis of typhoon-related ozone episodes in Hong Kong. J. Geophys. Res. Atmos. 110, 1–17.
Jenkin, M., Young, J., Rickard, A., 2015. The MCM v3.3.1 degradation scheme for isoprene. Atmos. Chem. Phys. 15, 11433–11459.
Li, Y., Shao, M., Lu, S.H., Chang, C.C., Dasgupta, P.K., 2010. Variations and sources of ambient formaldehyde for the 2008 Beijing Olympic games. Atmos. Environ. 44, 2632–2639.
Li, M., Shao, M., Li, L., Lu, S., Chen, W., Wang, C., 2014a. Quantifying the ambient formaldehyde sources utilizing tracers. Chin. Chem. Lett. 25, 1489–1491.
Li, X., Rohrer, F., Brauers, T., Hofzumahaus, A., Lu, K., Shao, M., Zhang, Y.H., Wahner, A., 2014b. Modeling of HCHO and CHOCHO at a semi-rural site in southern China during the PRIDE-PRD2006 campaign. Atmos. Chem. Phys. 14, 12291–12305.
Ling, Z.H., Zhao, J., Fan, S.J., Wang, X.M., 2017. Sources of formaldehyde and their contributions to photochemical O_3 formation at an urban site in the Pearl River Delta, southern China. Chemosphere 168, 1293–1301.
Liu, Y., Shao, M., Kuster, W.C., Goldan, P.D., Li, X., Lu, S., De Gouw, J.A., 2009. Source identification of reactive hydrocarbons and oxygenated VOCs in the summertime in Beijing. Environ. Sci. Technol. 43, 75–81.
Liu, Z., Wang, Y., Gu, D., Zhao, C., Huey, L., Stickel, R., Liao, J., Shao, M., Zhu, T., Zeng, L., Amoroso, A., Costabile, F., Chang, C., Liu, S., 2012. Summertime photochemistry during CAREBeijing-2007: RO_x budgets and O_3 formation. Atmos. Chem. Phys. 12, 7737–7752.
Lyu, X., Guo, H., Simpson, I., Meinardi, S., Louie, P., Ling, Z., Wang, Y., Liu, M., Luk, C., Wang, N., Blake, D., 2016. Effectiveness of replacing catalytic converters in LPG-fueled vehicles in Hong Kong. Atmos. Chem. Phys. 16, 6609–6626.
Mason, S., Field, R.J., Yokelson, R., Kochivar, M., Tinsley, M., Ward, D., Hao, W., 2001. Complex effects arising in smoke plume simulations due to inclusion of direct emissions of oxygenated organic species from biomass combustion. Journal of Geophysical Research Atmospheres 106, 12527–12539.
Su, W., Liu, C., Hu, Q., Zhao, S., Sun, Y., Wang, W., Zhu, Y., Liu, J., Kim, J., 2019. Primary and secondary sources of ambient formaldehyde in the Yangtze River Delta based on ozone mapping and profiler suite (OMPS) observations. Atmos. Chem. Phys. 19, 6717–6736.
Tan, Z., Lu, K., Jiang, M., Su, R., Wang, H., Lou, S., Fu, Q., Zhai, C., Tan, Q., Yue, D., Chen, D., Wang, Z., Xie, S., Zeng, L., Zhang, Y., 2019. Daytime atmospheric oxidation capacity in four Chinese megacities during the photochemically polluted season: a case study based on box model simulation. Atmos. Chem. Phys. 19, 3493–3513.
Tang, G., Chen, X., Li, X., Wang, Y., Yang, Y., Wang, Y., Gao, W., Wang, Y., Tao, M., Wang, Y., 2019. Decreased gaseous carbonyls in the North China plain from 2004 to 2017 and future control measures. Atmos. Environ. 218, 117015.
Wang, Y., Wang, H., Guo, H., Lyu, X., Cheng, H., Ling, Z., Louie, P., Simpson, I., Meinardi, S., Blake, D., 2017. Long-term O_3-precursor relationships in Hong Kong: field observation and model simulation. Atmos. Chem. Phys. 17, 10919–10935.
Wang, Y., Guo, H., Zou, S., Lyu, X., Ling, Z., Cheng, H., Zeren, Y., 2018. Surface O_3 photochemistry over the South China Sea: application of a near-explicit chemical mechanism box model. Environ. Pollut. 234, 155–166.
Wolfe, G., Kaiser, J., Hanisco, T., Keutsch, F., de Gouw, J., Gilman, J., Graus, M., Hatch, C., Holloway, J., Horowitz, L., Lee, B., Lerner, B., Lopez-Hilifiker, F., Mao, J.,

Marvin, M., Peischl, J., Pollack, I., Roberts, J., Ryerson, T., Thornton, J., Veres, P., Warneke, C., 2016a. Formaldehyde production from isoprene oxidation across NO_x regimes. Atmos. Chem. Phys. 16, 2597–2610.

Wolfe, G., Marvin, M., Roberts, S., Travis, K., Liao, J., 2016b. The framework for 0-D atmospheric modeling (F0AM) v3.1. Geosci. Model Dev. (GMD) 9, 3309–3319.

Xu, R., Li, X., Dong, H., Wu, Z., Chen, S., Fang, X., Gao, J., Guo, S., Hu, M., Li, D., Liu, Y., Liu, Y., Lou, S., Lu, K., Meng, X., Wang, H., Zeng, L., Zong, T., Hu, J., Chen, M., Shao, M., Zhang, Y., 2020. Measurement of gaseous and particulate formaldehyde in the Yangtze River Delta, China. Atmos. Environ. 224, 117114.

Xue, L., Gu, R., Wang, T., Wang, X., Saunders, S., Blake, D., Louie, P., Luk, C., Simpson, I., Xu, Z., Wang, Z., Gao, Y., Lee, S., Mellouki, A., Wang, W., 2016. Oxidative capacity and radical chemistry in the polluted atmosphere of Hong Kong and Pearl River Delta region: analysis of a severe photochemical smog episode. Atmos. Chem. Phys. 16, 9891–9903.

Yang, X., Xue, L., Yao, L., Li, Q., Wen, L., Zhu, Y., Chen, T., Wang, X., Yang, L., Wang, T., Lee, S., Chen, J., Wang, W., 2017. Carbonyl compounds at Mount Tai in the North China plain: characteristics, sources, and effects on ozone formation. Atmos. Res. 196, 53–61.

Yang, X., Zhang, G., Sun, Y., Zhu, L., Wei, X., Li, Z., Zhong, X., 2020. Explicit modeling of background HCHO formation in southern China. Atmos. Res. 240, 104941.

Zeng, P., Lyu, X.P., Guo, H., Cheng, H.R., Wang, Z.W., Liu, X.F., Zhang, W.H., 2019. Spatial variation of sources and photochemistry of formaldehyde in Wuhan, Central China. Atmos. Environ. 214, 116826.

Zhang, K., Zhou, L., Fu, Q., Yan, L., Bian, Q., Wang, D., Xiu, G., 2019a. Vertical distribution of ozone over Shanghai during late spring: a balloon-borne observation. Atmos. Environ. 208, 48–60.

Zhang, Y., Xue, L., Dong, C., Wang, T., Mellouki, A., Zhang, Q., Wang, W., 2019b. Gaseous carbonyls in China's atmosphere: tempo-spatial distributions, sources, photochemical formation, and impact on air quality. Atmos. Environ. 214, 116863.

Zhang, K., Li, L., Huang, L., Wang, Y., Huo, J., Duan, Y., Wang, Y., Fu, Q., 2020. The impact of volatile organic compounds on ozone formation in the suburban area of Shanghai. Atmos. Environ. 232, 117511.

Zhang, K., Huang, L., Li, Q., Huo, J., Duan, Y., Wang, Y., Yaluk, E., Wang, Y., Fu, Q., Li, L., 2021. Explicit modeling of isoprene chemical processing in polluted air masses in suburban areas of the Yangtze River Delta region: radical cycling and formation of ozone and formaldehyde. Atmos. Chem. Phys. 21, 5905–5917.

Zhu, J., Wang, S., Wang, H., Jing, S., Lou, S., Saiz-Lopez, A., Zhou, B., 2020. Observationally constrained modeling of atmospheric oxidation capacity and photochemical reactivity in Shanghai, China. Atmos. Chem. Phys. 20, 1217–1232.